



Microfluidic shear rheology and wall-slip of viscoelastic fluids using holography-based flow kinematics

Cite as: Phys. Fluids **32**, 012006 (2020); <https://doi.org/10.1063/1.5135712>

Submitted: 08 November 2019 . Accepted: 31 December 2019 . Published Online: 21 January 2020

Siddhartha Gupta , and Siva A. Vanapalli 



View Online



Export Citation



CrossMark

ARTICLES YOU MAY BE INTERESTED IN

[Microfluidic viscometers for shear rheology of complex fluids and biofluids](#)

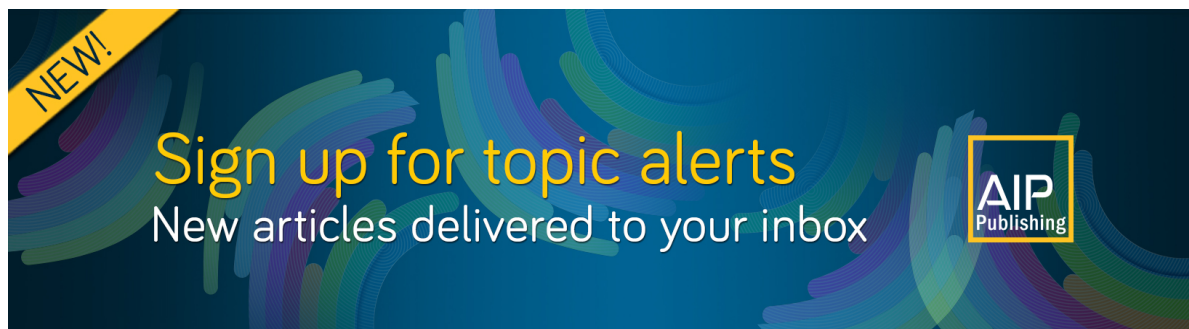
Biomicrofluidics **10**, 043402 (2016); <https://doi.org/10.1063/1.4955123>

[Invited contributions from outstanding early career researchers](#)

Physics of Fluids **32**, 010401 (2020); <https://doi.org/10.1063/1.5143523>

[Relaxation time of dilute polymer solutions: A microfluidic approach](#)

Journal of Rheology **61**, 327 (2017); <https://doi.org/10.1122/1.4975933>



Microfluidic shear rheology and wall-slip of viscoelastic fluids using holography-based flow kinematics

Cite as: Phys. Fluids 32, 012006 (2020); doi: 10.1063/1.5135712

Submitted: 8 November 2019 • Accepted: 31 December 2019 •

Published Online: 21 January 2020



Siddhartha Gupta  and Siva A. Vanapalli^{a)} 

AFFILIATIONS

Department of Chemical Engineering, Texas Tech University, Lubbock, Texas 79409, USA

^{a)}Email: siva.vanapalli@ttu.edu

ABSTRACT

In this study, we report microfluidic shear rheology and wall-slip using the 3D-resolved flow kinematics obtained from digital holography microscopy (DHM). We computationally reconstruct the recorded holograms to visualize the tracer imbued flow volume in linear microchannels, followed by the implementation of particle tracking velocimetry (PTV) to quantitate spatially resolved velocity fields in 3D. In order to select optimal parameters for DHM-PTV characterization of viscoelastic fluids, we studied the effect of the hologram recording distance, seeding density, and particle size. Using the optimal parameters, we show quantitative characterization of the shear rheology from the velocity fields without any *a priori* assumptions of wall boundary conditions or constitutive equation. The viscosity vs shear rate data for Newtonian and polyethylene oxide (PEO) solutions could be measured in the range of ≈ 0.05 to $20\,000\text{ s}^{-1}$ with just three input pressures using sample volumes as low as $20\text{ }\mu\text{l}$. These data from holographic shear rheometry were found to be in good agreement with computational fluid dynamics simulations and macrorheometry. With respect to the wall-slip, we find that highly viscoelastic PEO solutions can show slip lengths in the order of few microns. Finally, we discuss holographic visualization of particle migration in microfluidic flows, which can limit flow field access, whereas at the same time provide a fingerprint of the suspending fluid rheology.

Published under license by AIP Publishing. <https://doi.org/10.1063/1.5135712>

I. INTRODUCTION

Numerous applications have emerged, especially with biofluids, where there is a need to characterize nonlinear rheological properties using only limited sample volumes. This need combined with advances in microfluidics has led to miniaturized rheometers.^{1–3} Microfluidic devices offer an exquisite control of channel geometry and access to unique flow regimes for the characterization of viscoelastic fluids. Indeed, several studies have shown microfluidic determination of shear^{4–6} and extensional^{7–9} rheological properties of viscoelastic fluids.

Microfluidic rheometers often quantitate shear rheology by measuring the relationship between the pressure drop and flow rate relation in linear microchannels.^{6,10,11} Although such approaches enable the determination of material properties, they do not provide information on the flow structure or slip, which can become important when fluids shear band¹² or when channel walls are nonwetting. The presence of shear-banding or slip complicates the interpretation

of the pressure-drop vs flow rate relation for quantitating fluid rheology. Additionally, the measurement of the pressure drop or flow rate requires sensors that are in contact with the fluid, which might be problematic when the use-and-throw capability of microfluidic devices is desired with biofluids.

The integration of optical techniques into microfluidic flows have the potential to address the above limitations since they can characterize flow kinematics and, moreover, are noncontact.^{10,13,14} Ideally, these techniques should be capable of accessing flow information in 3D, i.e., the three spatial dimensions due to the rectangular cross-section of microfluidic geometries, as well as with fast temporal resolution. Particle imaging velocimetry and confocal microscopy provide access to 3D resolved velocity fields but require mechanical scanning through the flow volume and the set ups are bulky and expensive.

For characterizing kinematics in 3D, digital holography microscopy (DHM) is well suited since it is a volumetric imaging technique that does not require mechanical scanning and allows

fast temporal resolution.¹⁵ Holograms are reconstructed, and computational scanning is performed to localize seeded particles in 3D.¹⁶ Particle-tracking velocimetry (PTV) is then used to obtain 3D resolved velocity fields. This DHM-PTV has been previously used for micromixer flows,¹⁷ dean flows,¹⁸ flows on patterned surfaces,¹⁹ colloidal dynamics,^{20,21} microchannel flows,^{22–24} and turbulence.^{25,26}

Most prior studies of DHM-PTV have focused on Newtonian flows and its application to viscoelastic flows in microfluidic geometries is emerging. Shear banding and flow fluctuations due to wormlike micellar fluids in rectilinear microchannels have been studied using DHM-PTV.¹² In addition, viscoelastic flow around a confined cylinder has been mapped using DHM-PTV.²⁷ More recently, DHM-PTV was used to characterize 3D velocity fields in a hyperbolic contraction-expansion geometry.²⁸

In this study, we apply DHM-PTV to the flow of viscoelastic polymeric fluids in linear microchannels and show that shear rheology can be directly obtained from the measured 3D velocity fields and imposed driving pressure. This approach referred to as Holographic Shear Rheology (HSR), not only measures nonlinear rheology of fluids, but also informs about the presence of wall-slip and provides insights into viscoelastic particle migration. The shear viscosity curves from HSR are found to be in quantitative agreement with macrorheometry. Thus, HSR measures shear rheology of viscoelastic fluids without explicitly obtaining pressure drop and flow rate relation, but also provides quantitative information on wall-slip and flow structure.

II. WORKING PRINCIPLE OF HOLOGRAPHIC SHEAR RHEOLOGY

To characterize the shear rheology of viscoelastic fluids, we employ holography-based particle-tracking velocimetry. The basic idea is to impose a known pressure drop on a thin microchannel and obtain velocity profiles using DHM-PTV. This enables the calculation of shear stress vs shear rate relation, from which viscosity curves can be generated. In this section, we discuss this approach that forms the basis of our holographic shear rheology (HSR). First, we present the governing equations for quantitating shear rheology from velocimetry data. Second, we describe the details of the implementation of the DHM-PTV analysis pipeline to obtain velocity fields.

A. Quantification of shear rheology from velocimetry data

To determine shear rheology, we consider viscoelastic flow through a linear microchannel of length L_{ch} , height h , and width w . Our analysis follows that of Ref. 29. Ignoring external body forces and applying the Cauchy momentum equation gives $\frac{Du}{Dt} = \frac{1}{\rho} \nabla \cdot \sigma$, where $\frac{D}{Dt}$ is the material derivative, u is the local fluid velocity, ρ is the fluid density, and $\nabla \cdot \sigma$ is the divergence of the stress tensor. When the channel aspect ratio is small such that $h/w \ll 1$, and for steady unidirectional flow, the Cauchy momentum equation simplifies to $\frac{\partial \sigma_{xz}}{\partial z} = \frac{\partial P}{\partial x} = \frac{\Delta P}{L_{ch}}$, where x and z are the streamwise

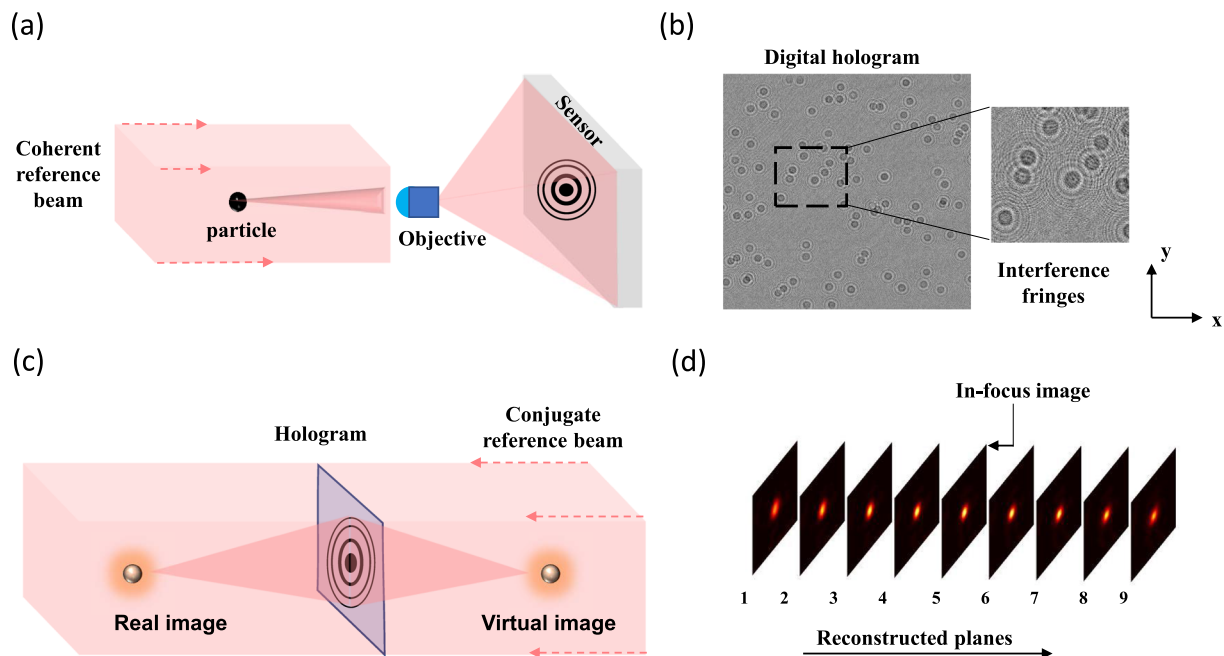


FIG. 1. Principle of Digital Holography Microscopy (DHM). (a) Digital hologram recording on a digital sensor with collimated laser beam. The interference between the reference beam and forward scattering from the particle leads to interference fringe patterns. The fringes are magnified by a microscope objective prior to recording on the sensor. (b) Cleaned hologram of dilute particle (diameter = $2\ \mu\text{m}$) suspension flowing in a PDMS microslit recorded at $20\times$ magnification and at $512\ \mu\text{m} \times 512\ \mu\text{m}$ field of view. Inset shows zoomed-in fringe patterns. (c) Principle of digital reconstruction of object field from the recorded hologram. The conjugate of the reference beam is numerically imposed on the recording, and convolution with a transfer function yields reconstruction of the 3D volume. (d) Planewise reconstruction of the intensity of a particle in the image volume.

and depthwise coordinates, respectively, and $\frac{\partial P}{\partial x}$ is the streamwise pressure gradient that can be determined from the known imposed pressure drop ΔP . Upon integration, the local shear stress becomes: $\sigma_{xz} = \left(\frac{\Delta P}{L_{ch}}\right)(z - z_{\dot{\gamma}=0})$, where $z_{\dot{\gamma}=0}$ indicates the plane of zero shear stress (or maximum velocity), which may not be at the midplane in the presence of slip events. The local shear rate can be determined from the measured depthwise velocity profile as $\dot{\gamma}_z = \frac{\partial u_x}{\partial z}$. Thus, knowing the shear stress vs the shear rate data, shear viscosity curves can be determined since shear viscosity $\mu = \frac{\sigma_{xz}}{\dot{\gamma}_z}$.

The above analysis has parallels to that of slit or capillary rheometry,³⁰ where pressure drop vs flow rate relations are used to quantitate shear rheology. Microfluidic viscometers also use such relations to characterize shear rheology.^{2,6,31} In HSR, we do not measure the volumetric flow rate but instead calculate local velocity gradients from the velocity profile. As a result, in situations where wall-slip is present, viscometers that rely on the measuring volumetric flow rate can be prone to error. However, wall-slip does not affect the HSR approach since the local shear rate is obtained rather than calculating the mean shear rate from the flow rate. The importance of wall-slip in viscoelastic microflows is further discussed in Sec. IV D.

B. Implementation of the DHM-PTV analysis pipeline

To characterize the velocity profiles of viscoelastic fluids, we developed a DHM-PTV analysis pipeline that consists of the following steps: (i) the fluid is seeded with nondeformable microparticles, (ii) inline holography records the tracer imbued volume as 2D holograms, (iii) the scattering field of individual particles in the flowing volume is recovered by digital reconstruction, (iv) particle centroid locations in 3D are identified in the image volume, and (v) trajectories are linked framewise using PTV³² and the velocity field is determined. A detailed explanation of these different steps is provided below:

1. Inline recording of digital holograms

The inline digital hologram recording is done by illuminating the sample space with a coherent reference beam of collimated laser light and recording the forward interference patterns on a sensor located perpendicular to the reference beam [Fig. 1(a)]. The forward scattering from the object, i.e., the object wave and the reference wave interfere in the focal plane of the microscope objective located beyond the sample volume and gets recorded as fringe patterns [Fig. 1(b)]. Holograms are magnified by a microscope objective, prior to recording to enhance fringe resolution and improve the depthwise accuracy during reconstruction. The intensity distribution of the raw hologram is denoted as $I_{i,raw}(x_h, y_h)$, where x_h, y_h denote pixel coordinates on the 2D image, and i is the index corresponding to the hologram number in the recorded video.

2. Digital reconstruction of the particle scattering field

The raw holograms are digitally reconstructed by computationally imposing a conjugate reference beam and calculating the forward scattering [Fig. 1(c)]. This process effectively provides 3D visualization of the flow volume with particles appearing as bright scattering regions against the external background. Operationally,

there are two steps for the digital reconstruction process. First, individual raw holograms are cleaned by removing noise using a background hologram that is obtained by averaging a sequence of typically 100 holograms. Mathematically, the cleaning process can be written as, $I_{i,clean} = I_{i,raw} - I_{bgrd}$, where the intensity distribution of the background hologram $I_{bgrd} = \frac{1}{N} \sum_{i=1}^N I_{i,raw}$. The background subtracted hologram is free from static noise and is subsequently referred to as the cleaned hologram. Second, reconstruction is done on the cleaned holograms using the angular spectrum method as it does not have a minimum distance requirement^{17,33} and allows computationally efficient reconstruction with an improved signal to noise ratio.^{34,35} Under the angular spectrum method, the field propagation is expressed as a linear filtering of the angular spectrum of the original field. The reconstructed complex amplitude $A_i(x, y, z)$ is obtained by convolving the cleaned hologram $I_{i,clean}(x_h, y_h)$ with the free space transfer function $h_z(x, y, z; x_h, y_h)$,^{33,36–38} i.e.,

$$A_i(x, y, z) = I_{i,clean}(x_h, y_h) \otimes h_z(x, y, z; x_h, y_h). \quad (1)$$

Here, x and y denote the spatial coordinates in the reconstructed plane (which are also the same as the spatial coordinates in the flow), and z indicates the depthwise position of the reconstruction plane. The convolution is implemented using Fast Fourier Transform (FFT) based calculations as

$$A_i(x, y, z) = \mathcal{F}^{-1}[\mathcal{F}(I_{i,clean}(x_h, y_h))X\mathcal{F}(h_z(x, y, z; x_h, y_h))]. \quad (2)$$

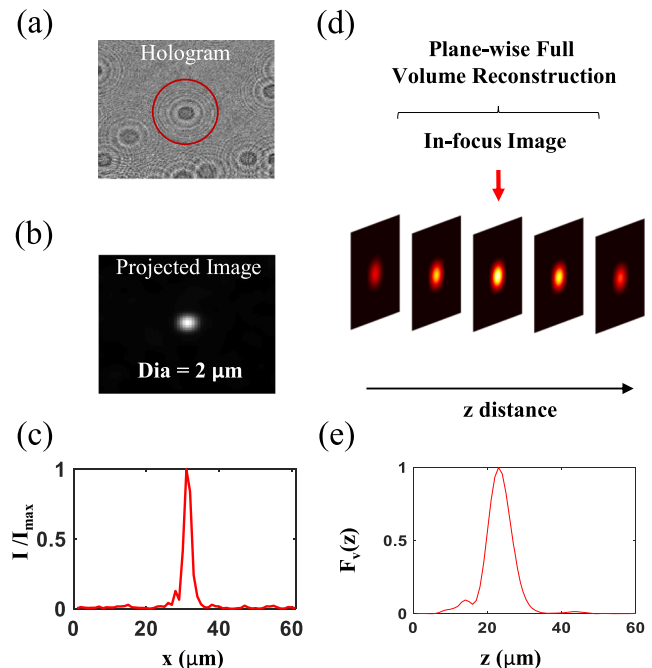


FIG. 2. Locating the particles in three dimensions. (a) A particle is identified in a cleaned hologram. (b) The reconstructed planes are projected in a 2D image that is used to segment the objects as regions of bright intensity. (c) The peak lateral intensity profile (I/I_{max}) is used to get the planar centroid location of the particle. (d) The full planewise stack of the intensity volume is reconstructed. (e) The Laplacian of the axial intensity $F_v(z)$ is calculated along the depth, and its maxima is used to determine the z location of the particle centroid.

Here, \mathcal{F} and \mathcal{F}^{-1} denote the FFT and inverse FFT, respectively. The intensity distribution corresponding to the 3D particle field is then calculated as $I_{i,volume}(x, y, z) = |A_i(x, y, z)|^2$, which is shown in Fig. 1(d) as a series of reconstructed planes.

3. Particle localization in 3D space

The reconstructed planes are used to locate the centroids (x_c , y_c , z_c) of the particles in 3D. To determine the (x_c , y_c) location of a particle in the raw hologram [Fig. 2(a)], the maximum intensity at every pixel coordinate is obtained by scanning all the planes and projecting onto a 2D image [Fig. 2(b)]. The peak in the intensity profile of the projected image [Fig. 2(c)] is identified as (x_c , y_c). To identify the z -coordinate of the centroid, the plane of the best focus is determined. This is done by performing a Laplacian operation on the intensity distribution in the image volume [Fig. 2(d)], i.e., $F_v(z) = \sum_{x,y} (\nabla^2 I_{i,volume}(x, y, z))^2$, with the summation carried over a 3×3 -pixel grid around the (x_c , y_c) location in each reconstruction plane. The plane of focus is chosen as the plane where $F_v(z)$ is maximized, and the z -location of this focal plane is chosen as z_c [Fig. 2(e)]. Thus, the tracer particles in the flow volume are localized in 3D.

4. Particle tracking velocimetry to obtain velocity field

Once particle centroids are established, we map the tracer displacement field by evaluating trajectories with PTV. The PTV algorithm used in this study is based on calculating velocity gradient tensors (VGT) as proposed by Ishikawa *et al.*, which was chosen for its suitability to map 3D flows.^{32,39} The basic idea entails estimating the flow feature for a parent particle having a local neighborhood by correlating it with a possible candidate in the next frame having a similar neighborhood and calculating the velocity gradient tensor matrix between the two particles in the respective frames. Briefly, a parent particle x_I is chosen in the first frame and potential candidates x_J for linking trajectories are found in the next frame within a search radius R_s [Fig. 3(a)]. Next, a cluster of the neighborhood radius R_n is formed around the first frame particle having neighbors x_{in} , where n denotes the index of the neighbor, and similar clusters are assumed around the candidates x_J in the second frame [Fig. 3(b)] having neighbors x_{jn} . The choice of R_n is made to retain at least 2–3 particles in each cluster and every cluster pair is evaluated by calculating the VGT tensor via a least square's minimization approach. The minimization exercise is formulated as

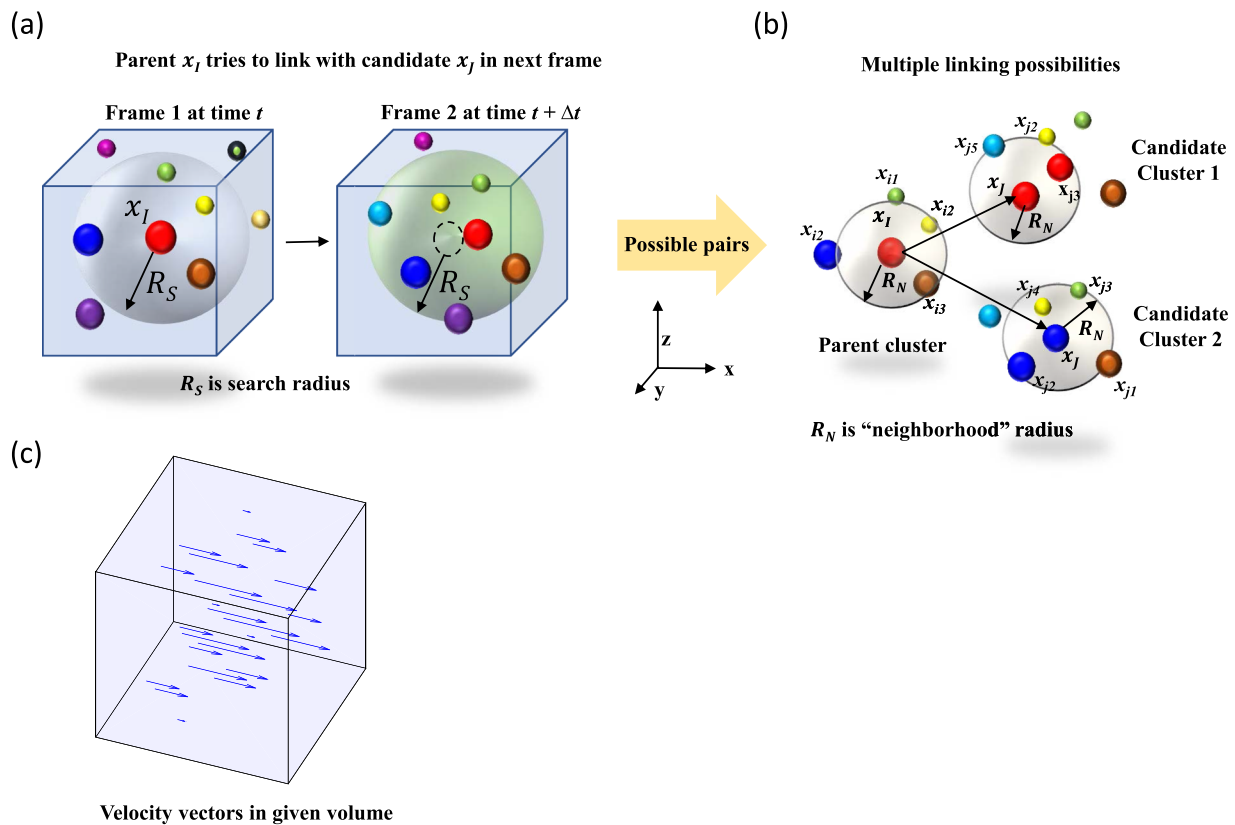


FIG. 3. The particle tracking velocimetry approach is based on the method proposed by Ishikawa *et al.*, 2000.³² (a) First, a parent particle x_I is chosen in frame 1 at time t and an attempt to link its trajectory is made by finding it in the next frame at time $t + \Delta t$ as candidate x_J within a search radius R_s . (b) Multiple linking possibilities arise in cases of multiple candidate particles in the search radius R_s . A cluster of search radius R_n is identified around the parent and its candidates in the next frame and all the participants of the cluster pair are linked piecewise to obtain the velocity gradient tensor matrix for each combination. The most probable link is estimated using a least squares minimization strategy. (c) The trajectories from the pairings are stored as coordinates of the tail and the head of the displacement vector.

$$E_{IJ} = \sum_{k=1}^n |X_{J,K} - AX_{IK}|^2. \quad (3)$$

Here, the matrix $A = I + \partial u(x_I) \Delta t$ includes the velocity gradient tensor $\partial u(x_I)$ and the unit matrix I , and $X_{J,K}$ and $X_{I,K}$ are distances of cluster centers from their neighbors. The best possible pairing is decided by the minimal value of E_{IJ} . The pairings are stored as tail and head coordinates of the trajectory displacement vector [Fig. 3(c)].

5. Postprocessing of velocity vector data

The DHM-PTV output is susceptible to statistical noise intrinsic to the linking process, fringe distortion at walls, and noisy reconstruction. Additionally, vector generation is sensitive to particle distribution within the flow, which can be sparse. Therefore, we construct a regular grid aligned with the flow cross-section to project the PTV velocity vector data. The projection is consistent with steady state flow invariance in the streamwise direction. The PTV data are median and gaussian filtered to remove outliers before interpolation onto the uniform grid for the calculation of the flow field. Each velocity vector within a grid element is ascribed to the center and only those grid cells are considered, which contain at least 8–12 velocity vectors inside the grid element.

III. EXPERIMENTAL METHODS

A. Digital holography microscopy

The inline digital holography microscopy setup used in this study, including the optical train and imaging system, is the same as that of our previous works.^{40,41} The holograms of the microchannel flow are recorded in the focal plane of a 20× magnification microscope objective (NA = 0.45, Olympus). The magnified fringe patterns from the hologram are captured using a CMOS camera (Phantomv310, Vision Research) with a field-of-view (FOV) of 512 × 512 pixels. This imaging system yields a resolution of 1 μm per pixel, indicating that the lateral spatial resolution is ±1 μm. An exposure time of 9–11 μs was employed, and the frame rate (24–11 001 fps) was controlled so that the fastest particle traversed 5–40 pixels between frames. The recording distance, i.e., the distance between the microchannel floor and the focal plane of the microscope objective was maintained at 100 μm unless otherwise stated.

Holographic reconstruction was done with an interplane spacing of 1 μm, imposing a fundamental limit of ±1 μm on the depthwise resolution. Although accurate velocity fields were obtained from ~1000 holograms, we recorded and analyzed ~10 000 holograms to improve PTV statistics, especially when sparse particle fields can be present in the channel domain due to particle migration in viscoelastic flows, as further discussed in Sec. IV D. The hologram processing and PTV analysis were performed using custom routines with parallel computing capability written in MATLAB (MathWorks). Computational processing was done on a desktop (XPS 8930, Dell Inc.) running Windows OS on multiple cores (Intel Core i7-8700K CPU @ 3.70 GHz, 3696 MHz, 6 Cores). Each hologram pair required ~2 s processing time (this includes reconstruction and PTV analysis). A 10 000 hologram video required 7 h of computational time to yield velocity vector data.

B. Sample preparation

The choice of the Newtonian test fluid was deionized (DI) water. For polymeric fluids, polyethylene oxide (PEO) of a reported molar mass of 4×10^6 g/mol (WSR301, DOW) was used, which had an overlap concentration $c^* \sim 620$ ppm.⁴² A semidilute stock polymer solution of 1 wt. % was prepared by dissolving PEO in DI water and stirring at 85 rpm for 48 h using a magnetic stir bar. The stock solution was stored at 4 °C wrapped in an aluminum foil to prevent photodegradation. The stock was thence diluted serially to 0.5, 0.25, and 0.025 wt. % prior to experiments. Our optimal seeding density for the test fluids was ~0.14 v/vol. % (or 9×10^6 particles/ml) for polystyrene microspheres of diameter 2 μm (density 1.05 g/cm³, PS 19814-15, Polysciences). This resulted in a particle number density of ~100 particles in the FOV for the thin-slit microchannel and ~50 particles for the microchannel with the square cross-section. To evaluate the effect of the particle size on DHM-PTV performance, we also tested particles of 3 μm (PS 17134-15, Polysciences) and 6 μm (PS 07312, Polysciences) diameter.

C. Rheological characterization

The shear viscosity curves for all the PEO solutions were measured on a macrorheometer (AR2000, TA instruments) using the double gap geometry at the temperature (21–23 °C) of the microfluidic flow experiments. In addition, their relaxation time was determined by dripping-on-substrate rheometry⁴³ and our setup for this measurement is identical to that reported recently.²⁸ The measured relaxation times for 1, 0.5, 0.25, and 0.025 wt. % PEO solutions were 240.1 ± 20.5 , 182 ± 18 , 55 ± 3.9 , and 7.1 ± 0.15 ms, respectively.

D. Microfluidic device fabrication

The experiments were done in linear microchannels with thin-slit (rectangular) and square cross-sections. To fabricate the microfluidic channels, we used SU8-based soft lithography.⁴⁴ Negative photomasks designed in AutoCAD were printed. Next, an SU-8 mold was made using soft lithography on a 3" silicon wafer. The height of the channels was controlled during the spin coating process and was targeted to be 50 μm for the 500 μm wide thin-slit and 100 μm for the square channel. Polydimethylsiloxane (PDMS) was prepared by mixing a crosslinker and base (Sylgard-184 Silicone Elastomer kit, DOW) in a 1:10 wt. % ratio and degassed before being poured on the SU-8 mold. The mold was cured in an oven for 5–6 h at 65 °C after which the PDMS chips were peeled off and characterized using a microscope (CKX41, Olympus) to determine the height variation. Post characterization, the height of the thin-slit microchannel was found to be ~44 μm and width 500 μm, whereas, for the square microchannel, the height was found to be 103 μm and the width to be 105 μm. The error in these spatial dimensions corresponds to the optical resolution of ±1 μm. Inlet and outlet reservoirs were defined by punching holes, and the channels were irreversibly bonded to a glass slide (25 mm × 75 mm × 1 mm, Fisher) after exposing the bonding surfaces of the PDMS device and glass slide to plasma (Harrick Plasma) for 2 min.

E. Flow experiments

For HSR experiments, constant pressure at the inlet of the microfluidic devices was imposed using a pressure controller

(MFC8-FLEX4C, Fluigent, Inc.). The pressure drop across the device was varied discretely from 0 to 355 mbar. For validating the flow kinematics, a constant volumetric flow rate of 500 $\mu\text{L/h}$ was imposed onto the thin-slit and square microchannel devices using syringe pumps (PHD2000, Harvard Apparatus). After starting the flow, a stabilization time of ≈ 2 –10 min was allowed.

For the flow conditions used in the study, the Reynolds number varied from $Re \approx 10^{-5}$ to 32. Due to the shear-thinning nature of the PEO solutions, we defined $Re = \frac{\rho \bar{v}^{2-n} D_H^n}{K \left(\frac{3n+1}{4n} \right)^n 8^{n-1}}$, where \bar{v} is the average flow velocity, K (Pa s^n) is the power law prefactor, and n is the power law exponent.⁴⁵ In our study, the Weissenberg number varied from $Wi \sim 1$ –161, with $Wi = \lambda \dot{\gamma}_c$, where $\dot{\gamma}_c (= \frac{2\bar{v}}{h})$ is the characteristic shear rate, and λ is the relaxation time of the fluid. Finally, the elasticity number defined as $El = \frac{Wi}{Re}$ varied from ≈ 3.5 to 10^4 .

DHM imaging was performed at $\approx 115D_H$ and $\approx 100D_H$ for the thin-slit and square microchannel geometries, respectively, which is sufficient for flow stabilization at the Reynold's numbers of our experiments.⁴⁶ Here, D_H is the hydraulic diameter of the microchannel. The minimum entrance length for achieving fully developed flow for Newtonian flow can be determined as $L_e = D_H \left(\frac{0.6}{1+0.035Re} + 0.056Re \right)$.³⁰ Since viscoelastic flows have a shorter entrance length than Newtonian flows,⁴⁷ we evaluate the entrance length at the highest Reynolds number ($=32$) used in our experiments, which gives an upper limit of $L_e \approx 2D_H$ for the square and the thin slit geometries. Since, our holograms are recorded at $\approx 115D_H$ and $\approx 100D_H$ for the thin-slit and square microchannel geometries, our development length is $\approx 2\%$ of the distance from the entrance where experiments are conducted.

F. Computational fluid dynamics

To validate the velocity profiles obtained from DHM-PTV, we performed finite volume-based simulations using the computational fluid dynamics (CFD) package Fluent (Ansys). The CFD simulations were validated against analytical expressions for Newtonian fluid in both the thin-slit and square microchannels to optimize meshing and model setup. The power-law fluid model was used to simulate the viscoelastic flow in the microchannels, and the resulting velocity profiles were compared with those obtained from DHM-PTV.

IV. RESULTS AND DISCUSSION

A. Optimization of system parameters for DHM-PTV

Successful determination of the 3D velocity profiles requires optimization of system parameters, which might include those from the holography setup as well as those pertaining to PTV analysis. Here, we considered experimental optimization of the following system parameters: the recording distance for the holograms, particle size, and particle concentration. The optimization was pursued by keeping one parameter fixed and varying the other two and evaluating the degree of error ΔV_{rms} between the measured and the theoretical velocity profile for a Newtonian fluid in a microchannel [see Eq. (4), where \dot{Q} is the flow rate]. Here, ΔV_{rms} represents the root mean-squared (rms) error of the midplane widthwise velocity profile calculated from the measured values and the analytical result for flow in a rectangular channel.⁴⁸ To report the deviation, we express the rms error as a percentage using $\Delta V_{\text{rms}} \times 100/V_{\text{max}}$, with

V_{max} being the maximum fluid velocity. The widthwise profile was chosen for calculating the rms error since it has more measured values enabling better statistical comparison,

$$u_x(y, z) = \frac{\frac{48 \dot{Q}}{\pi^3 h w} \sum_{n, \text{odd}} \frac{1}{n^3} \left[1 - \frac{\cosh(n\pi \frac{z}{h})}{\cosh(n\pi \frac{z}{2h})} \right] \sin(n\pi \frac{y}{h})}{\left[1 - \sum_{n, \text{odd}} \frac{192h}{n^3 \pi^3 w} \tanh(n\pi \frac{w}{2h}) \right]}. \quad (4)$$

In this study, we used a thin-slit microchannel [Fig. 4(a)] and optimized the system parameters. The tested conditions shown in Figs. 4(b)–4(d) include recording distance $Z_{\text{rec}} = 100, 600, 1200 \mu\text{m}$; particle size $D_p \approx 2, 3, \text{ and } 6 \mu\text{m}$; and particles per frame (or image volume) $N_o \approx 50, 100, 300$. Below, we elaborate on the results from this optimization study.

1. Hologram recording distance

In a holography system, despite the large depth of the field afforded in comparison with conventional microscopy, the recording distance Z_{rec} needs to be optimized because small recording distances are susceptible to noise from twin image formation,⁴⁹ whereas large separation between the object and the hologram recording the plane position suffers from aberrations led by a finite numerical aperture (NA) objective. Moreover, in the case of microfluidic channel flows, light rays refract from the flow media as well as the glass substrate and subtend a reduced light cone on the hologram plane (FOV) as the distance from the object is increased, reducing the effective NA of the system.¹⁷ Thus, there is a need to select the optimal recording distance.

In Fig. 4(c), we show the measured midplane widthwise and depthwise velocity profiles obtained for fixed particle size $D_p = 2 \mu\text{m}$ and particle per frame $N_o \approx 100$, but varying $Z_{\text{rec}} = 100, 600, \text{ and } 1200 \mu\text{m}$. We calculated the rms error to be $\approx 2.5\%$ for $Z_{\text{rec}} = 100$ and $600 \mu\text{m}$; however, it increases to $\approx 10\%$ for $Z_{\text{rec}} = 1200 \mu\text{m}$ as reconstruction suffers from optical aberrations that arise due to the reduced angular range of light rays incident on the FOV as well as from using a finite NA objective.

2. Particle size

The particle size is important because, depending on the diameter D_p , the particle may lead or lag the flow^{50,51} and migrate toward the centerline or the wall.⁵² The finite size limits the closest approach to the wall restricting information access from slower streamlines. We measured the velocity profiles for three different particle sizes $D_p \approx 2 \mu\text{m}, 3 \mu\text{m}, \text{ and } 6 \mu\text{m}$, while maintaining $N_o \approx 100$ and $Z_{\text{rec}} = 100 \mu\text{m}$. We find that the rms error remains under 2.5% and does not vary significantly for the particle sizes considered (data not shown), although we observe that for $D_p \approx 6 \mu\text{m}$, only $<73\%$ of the channel depth could be probed due to the exclusion of slow streamlines and hydrodynamic resistance due to the increased particle size (confinement).^{50,51}

3. Particle seeding density

An important factor for successful DHM-PTV analysis is the particle seeding density since it impacts the shadow density and vector yield. The shadow density S_d refers to the degree to which scattering intensity or “shadows” from particles located in the 3D image volume overlap when projected onto a 2D frame.^{53,54} A measure of shadow density is $S_d = \frac{N_o(D_p)^2}{wL_{\text{fov}}}$, where w is the width of

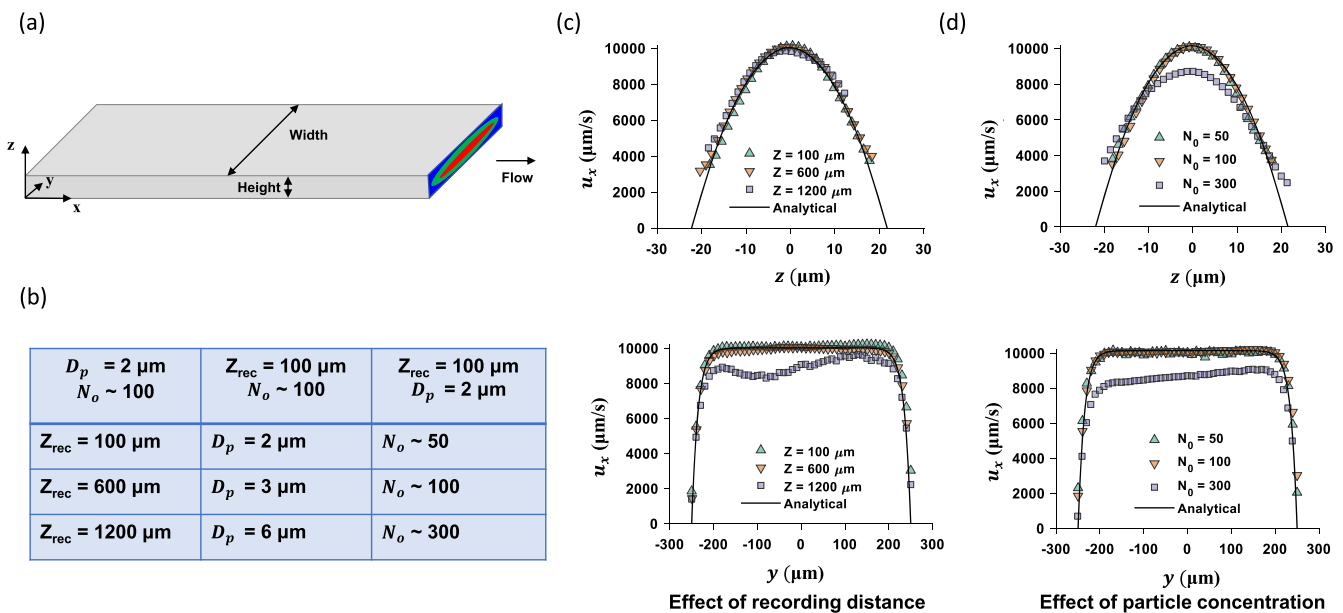


FIG. 4. Optimization of DHM-PTV in the thin slit. (a) Thin-slit microchannel geometry used for the optimization studies. (b) Three sets of trials were conducted for optimizing the DHM-PTV analysis, which include particle size D_p , particle number density N_o , and the recording distance Z_{rec} . The normalized rms error in velocity estimation from DHM PTV vs the analytical result for different trials: (c) the effect of the recording distance and (d) the effect of particle seeding density. In (c) and (d), the top and bottom panels are the depthwise and widthwise midplane velocity profiles. The flow rate is fixed at $500 \mu\text{l/h}$, corresponding to $\text{Re} = 0.59$.

the channel, $L_{\text{fov}} (=512 \mu\text{m})$ is the streamwise length of the field-of-view. It is clear that shadow density depends on the particles per frame N_o as well as particle size D_p . Here, we tested the influence of seeding density by maintaining, $D_p = 2 \mu\text{m}$ (and $Z_{\text{rec}} = 100 \mu\text{m}$), and varying $N_o \approx 50, 100$, and 300 . Under these conditions, S_d ranges from 0.08% to 0.48% . In general, the reconstruction efficiency decreases with increasing N_o or S_d .⁵⁴ In addition, this loss in reconstruction efficiency can lead to missing particles between frames hampering PTV vector yield. Alternatively, decreasing N_o significantly reduces the vector yield necessitating more holograms and greater processing times. Thus, there is a need for optimizing particle seeding density. The velocimetry results from this optimization are shown in Fig. 4(d). The velocity profiles deviate significantly from the analytical result for $N_o \approx 300$, yielding an rms error of 15% . In contrast, the rms error for $N_o \approx 50$ and ≈ 100 is less than 2.5% .

In summary, our optimization studies of system parameters revealed the conditions that yield the rms error of 2.5% or less. In this study, we chose $Z_{\text{rec}} = 100 \mu\text{m}$, $D_p = 2 \mu\text{m}$, and $N_o \approx 100$ particles per frame as the optimal operating parameters for DHM-PTV implementation.

B. Validation of DHM PTV for flow field characterization

To further validate that the optimal parameters have been identified for both Newtonian and viscoelastic fluids, we measured the 3D velocity profiles for water and 0.5 wt. \% PEO and compared them with Eq. (4) for Newtonian flows and CFD simulations for the case of viscoelastic flows. We performed these comparisons in both the

thin slit and square microchannels by imposing a constant flow rate and measuring the velocity profiles.

As shown in Figs. 5(a) and 5(b), the midplane velocity profiles for water in the spanwise and depthwise directions agree well with the analytical result from Eq. (4)⁴⁸ for a thin slit as well as square microchannel geometry. The maximum rms error for the thin-slit and square microchannel geometries is 2.5% and 3.4% , respectively, indicating little deviation from the analytical curves. The envelopes of 3D velocity profiles are also shown and display a distinct wedge-like appearance in the thin-slit and a paraboloid for the square microchannel.

Next, results for the flow of viscoelastic solution of 0.5 wt. \% PEO are shown in Fig. 6(a) for the thin-slit and for the square microchannel in Fig. 6(b). The viscoelastic flow exhibit a more blunted velocity front that departs from the parabolic Newtonian flow profiles due to shear thinning. Also, shown are the results from the CFD simulation using a power-law fluid model with K and n obtained from conventional rheometry. The maximum rms error is 1.9% and 3.8% for thin-slit and square microchannels, respectively, indicating that the experimental and simulation results are in good agreement. In addition, the level of error in the measured viscoelastic velocity profiles is comparable to that in the Newtonian fluid velocity profiles, indicating that the optimization of DHM-PTV parameters performed with Newtonian fluids in Sec. IV A also carries forward well to viscoelastic flow experiments.

We note that the depthwise velocity profiles truncate more than the spanwise velocity profiles in both the geometries and for both the fluids. In particular, the depthwise velocity profiles in the thin slit truncate markedly by ≈ 3 to $5 \mu\text{m}$ for Newtonian flows and ≈ 4 to $6 \mu\text{m}$ for viscoelastic flows from the channel roof and floor. The

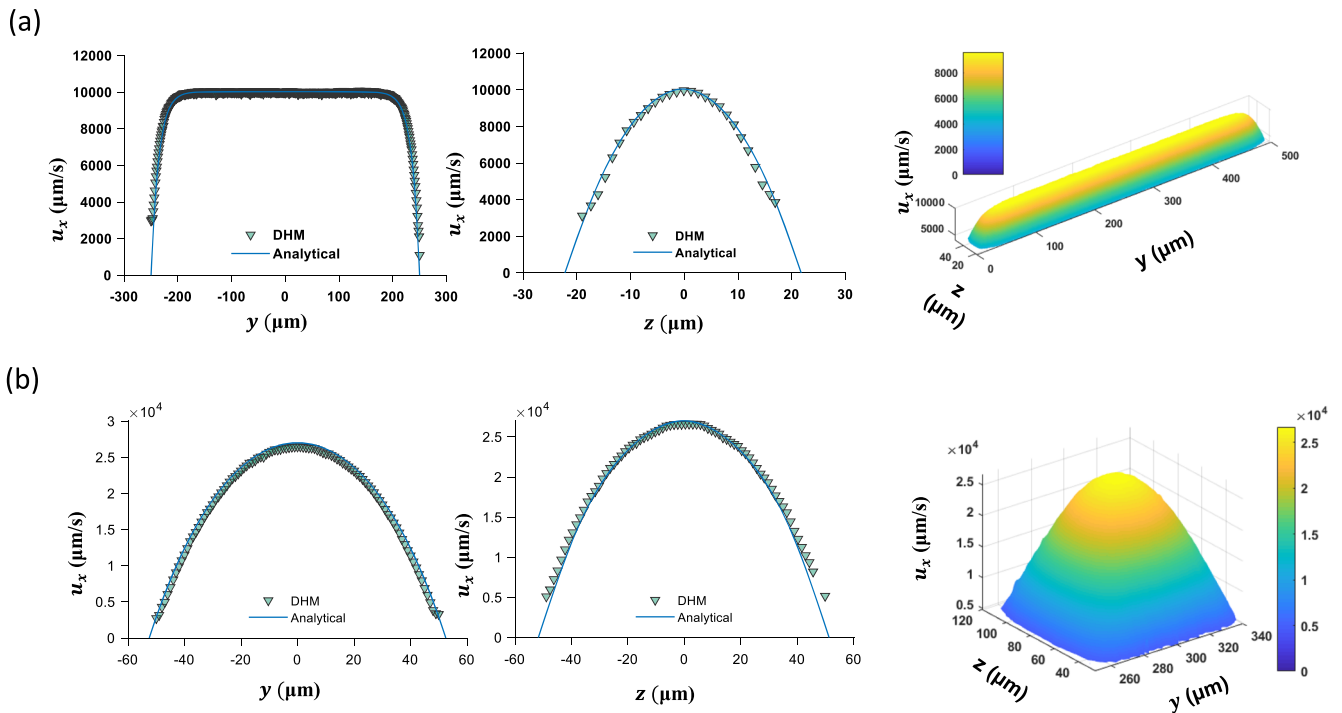


FIG. 5. 3D velocity profile of the Newtonian fluid. (a) The results for midplane velocity profiles along the height and width of the thin-slit channel alongside the 3D convex envelope of velocity over the flow cross-section ($Re = 0.59$). (b) Corresponding results in the case of a square microchannel ($Re = 1.38$). The color scale indicates velocity variation and the color bar has the same units as velocity in micrometer per second. The Newtonian fluid is water and the volumetric flow rate is $500 \mu\text{l/h}$.

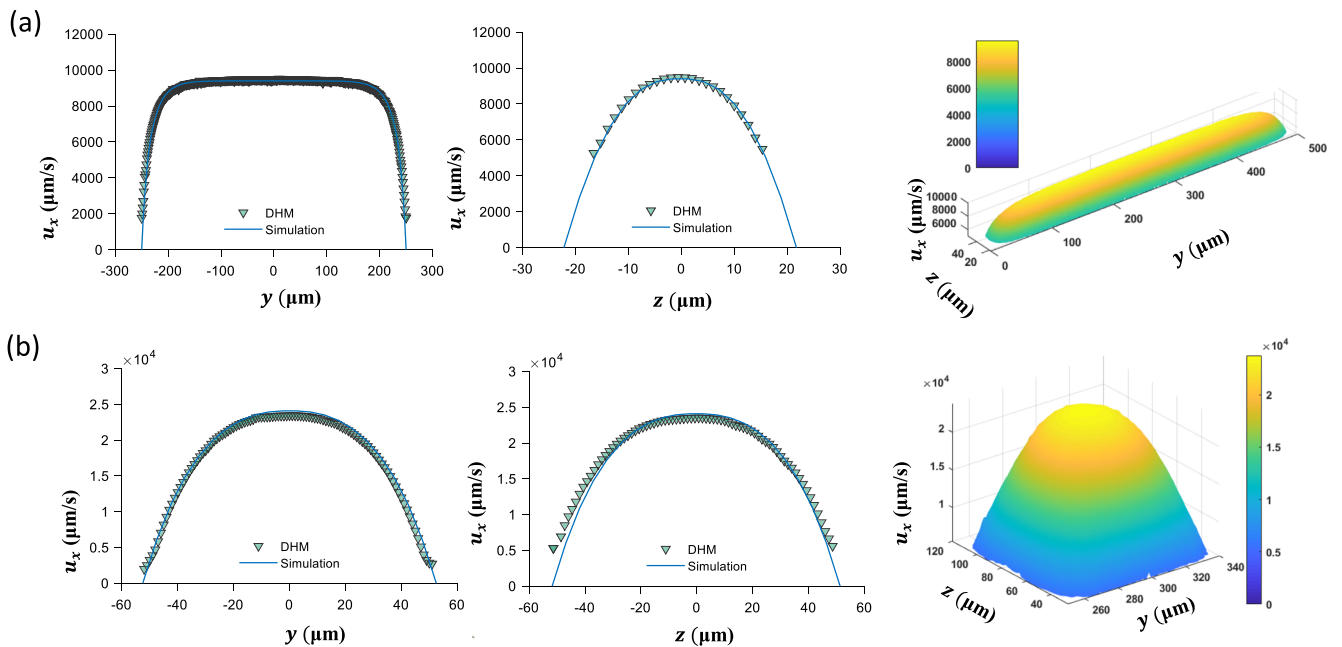


FIG. 6. 3D velocity profile for viscoelastic 0.5 wt. % PEO solution. (a) Midplane velocity profiles along the depth and width of the thin-slit channel alongside the 3D convex envelope of velocity over the flow cross-section ($Re = 0.038$, $Wi = 56$). (b) Corresponding results in the case of a square microchannel ($Re = 0.07$ and $Wi = 35$). The color scale indicates velocity variation, and the color bar has the same units as velocity in micrometer per second. The volumetric flow rate was fixed at $500 \mu\text{l/h}$.

reason for this truncation is due to sparse vector fields near the wall. As discussed further in Sec. IV D, we find that for the conditions explored in this study, particles migrate away from the walls,^{55–59} creating near-wall fluid regions that are sparsely populated with particles, making it difficult to faithfully extract velocity vectors close to the wall. Despite this limitation, as shown in Sec. IV C, the reliable shear viscosity curves can be obtained from the available flow kinematics data.

C. Holographic shear rheology from flow kinematics

To quantify shear rheology of viscoelastic fluids, we conducted experiments in the thin-slit geometry and imposed a constant pressure drop. The DHM-PTV analysis pipeline was used to obtain the depthwise velocity profile and the shear stress and shear rate were calculated as previously discussed in Sec. II A. The shear stress vs the shear rate data are shown in Fig. 7(a) for water as well as 0.25, 0.5, and 1 wt. % aqueous PEO solutions. This dataset was obtained from the midplane depthwise velocity profile. Considering the depthwise velocity profiles from other vertical planes within 100 μm of the symmetry plane yielded imperceptible differences. In Fig. 7(b), the corresponding shear viscosity vs the shear rate data are shown. The measured data are in good agreement with that obtained from standard rheometry for viscoelastic fluids, and literature values for water. Thus, our HSR approach is well-suited for characterizing the shear rheology of viscoelastic fluids.

To obtain the data shown in Fig. 7, we typically used three different inlet pressure conditions, with a single pressure condition yielding an order of magnitude variation in the shear rate. We find that the shear rates ranged from $\approx 0.05 \text{ s}^{-1}$ to $20\,000 \text{ s}^{-1}$, with the lowest shear rates accessible only for the high-viscosity fluids. With high-viscosity fluids, the depthwise velocity variation is gradual compared to the low-viscosity fluids enabling access to lower shear rates. It is interesting to note that in microfluidic viscometry approaches reported to date,² the flow rates need to be adjusted to small values to access low shear rates; however, in our HSR approach, this need is obviated since the shear rate is determined from the velocity variation.

With respect to sample consumption, HSR requires minimal amounts. For example, to obtain the data in Fig. 7, the sample volume imaged ranged from $\approx 4.5 \mu\text{l}$ to $8 \mu\text{l}$ per decade of the shear rate variation for the highly viscous 1 wt. % PEO over recording times ranging from $\approx 10 \text{ min}$ at the slowest flows to $\approx 0.5 \text{ min}$ at the

highest pressure driven flow. Similarly, for the lowest viscosity case of water, the sample consumption was $\sim 7 \mu\text{l}$ per decade of shear rate variation with times ranging from 1.4 s to 1 min. The overall sample consumption per decade of shear variations in our case after accounting for flow stabilization wait times is $< 20 \mu\text{l}$. In order to generate an entire flow curve over three orders of magnitude variation as shown in Fig. 7, our sample consumption is $< 100 \mu\text{l}$ and the time of experiment is $< 20 \text{ min}$.

We now discuss factors that are important in obtaining reliable HSR data. The shear rates in HSR are estimated by numerical differentiation of the digitally reconstructed data, which makes them sensitive to noise in regions where velocity changes steeply. As a result, the HSR approach requires robust characterization of velocity variation over small lengths. The smallest length scale is dictated by the 1 μm interplane spacing during reconstruction. This reconstruction granularity coupled with the marginal velocity changes near the peak of the velocity profile limits access to viscosity data as $\dot{\gamma} \rightarrow 0$.

Similarly, stress measurements rely on accurate identification of the location of minimum shear $z_{\dot{\gamma}=0}$. This can be problematic when there is significant deformation in the PDMS channel due to strong pressure-driven flow.⁶⁰ At the highest imposed pressures ($\approx 355 \text{ mbar}$), we observed a maximum channel deformation of $\approx 2\text{--}3 \mu\text{m}$ near the center of the thin slit, which correlates well with estimates from the analytical expression $h(x) = \frac{3}{2}h_0\left(1 + \frac{\alpha P(x)w}{Eh_0}\right)$, where $h(x)$ and h_0 denote the maximum deformed height and the undeformed height, $P(x)$ is the local pressure, E is the Young's modulus, and α is the proportionality constant.⁶¹ Nevertheless, we observe that the results from HSR are in good concordance with macrorheology, indicating that these small channel deformations do not strongly impact the HSR data. This is because we estimated our $z_{\dot{\gamma}=0}$ from the velocity field data rather than depending on postfabrication characterization of the channel geometry. Finally, we note that the noise in the estimation of shear stress and shear rate is independent of each other and can result in accumulated noise in the estimation of viscosity as it depends on the ratio of the two values.

In this work, we have highlighted several advantages of using DHM-PTV for microfluidic shear rheology including the approach being noncontact, with small sample requirements and unaffected by slip. However, there are some limitations for our DHM-PTV technique for shear rheology. It is applicable to only optically transparent fluids and in complex fluids where the mesoscale structures do not scatter light strongly compared to the seeded particles. In

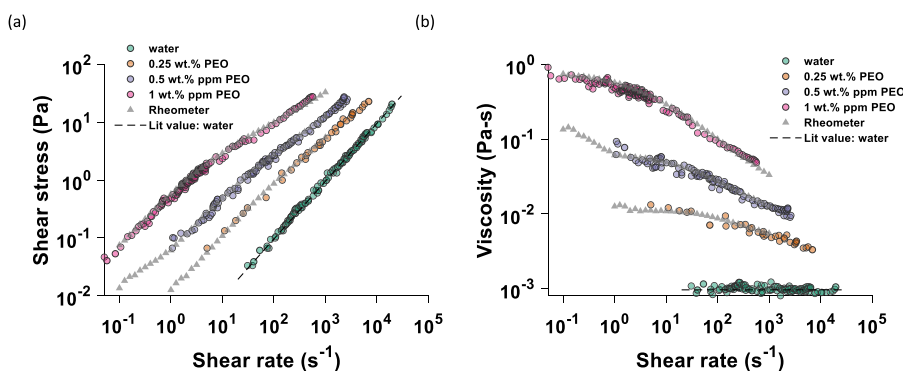


FIG. 7. Holographic shear rheology of water and viscoelastic PEO solutions. (a) Shear stress vs shear rate data obtained from DHM-PTV compared with rheometry data (triangles) for PEO solutions and with literature values for water (dashed line). (b) Viscosity vs the shear rate data for PEO solutions and water.

addition, our approach is limited to only shear rheology, whereas standard macrorheometers can impose a variety of stress/strain protocols to comprehensively probe complex fluid rheology.

D. Additional considerations for holographic shear rheology

In this section, we discuss two important effects that were apparent when performing holographic shear rheology. The first is associated with slip in viscoelastic flows and the second is particle migration in viscoelastic flows. Both these phenomena were observed under certain experimental conditions. Below, we describe results pertaining to these phenomena, which not only emphasize their importance in HSR, but also highlight that DHM-PTV is a powerful tool to analyze these phenomena in viscometric flows.

1. Wall slip in viscoelastic flows

In standard macrorheometry, the wall slip presents a problem for obtaining accurate rheological data and corrections need to be implemented.⁶² Since no assumptions about the wall boundary conditions are required in HSR, this method for determining shear rheology is indifferent to the presence of slip. Previously, the slip has been explored through variable-gap rheometry,⁶³ surface treatment,⁶⁴ particle tracking,⁶⁵ evanescent waves spectroscopy,⁶⁶ and rheo-NMR.⁶⁷ The chemical origins of slip can be attributed to molecular interactions between the fluid and the solid surface such as in polymer melts⁶⁸ or superhydrophobic surfaces⁶⁹ and its dynamics has been investigated for viscoelastic flows using PTV.⁷⁰ Here, we show that slip can occur under certain experimental conditions, and this slip can be characterized using DHM-PTV.

In our experiments, the microchannels were made with PDMS replicas bonded to glass slides. In these devices, the velocity profiles were characterized using DHM-PTV. The typical approach for determining the slip is to examine if there is truncation in the near-wall velocity profile. As discussed in Sec. IV D 2, in our experiments we observe depletion of seeded particles near the wall due to cross-flow migration in viscoelastic flows.⁵⁹ Therefore, we limit to velocity characterization beyond 3–5 μm away from the wall. Because of this limitation, we extrapolate near-wall information from the bulk by fitting to a power-law model as

$$v_z = \left(-\frac{\Delta P}{L_{ch}} \frac{h_{ext}}{K} \right)^{\frac{1}{n}} \frac{h_{ext}}{\left(\frac{1}{n} + 1 \right)} \left(1 - \left(\frac{z}{h} \right)^{\frac{1}{n} + 1} \right). \quad (5)$$

The depthwise velocity profile at the midplane is fitted to estimate the span h_{ext} for which the velocity extrapolates to zero. The apparent slip length is characterized as $\Delta h = (h_{ext} - h)$.

In Fig. 8(a), we show the results for the flow of water in a thin slit PDMS device bonded to glass at $\text{Re} = 1.3$ and 8. The midplane depthwise velocity profile extrapolates to zero on the PDMS top surface as well as the glass bottom, indicating the absence of slip behavior. However, when 1 wt. % PEO solutions was introduced in the same channel at different driving pressures such that $\text{Re} \approx 10^{-5}$, 10^{-4} and $\text{Wi} = 1.4, 7.2$ respectively, the velocity profiles extrapolated to zero at 3 μm and 5 μm beyond the glass boundary of the channel indicating an apparent sliplike behavior [Fig. 8(b)]. We note that due to viscoelastic particle migration, more velocity data are missing for PEO solution compared to that of water. Previously, Degre *et al.*²⁹ reported wall slip in flows of high molecular weight PEO solutions over a glass bottom surface similar to flow systems employed in this study.

Next, we coated the glass substrate with a 50 μm PDMS layer prior to bonding to check if a surface with different chemical interactions with PEO might alter the slip behavior observed with the glass surface. In this experiment, the bottom surface was fixed at the same distance from the microscope objective as the uncoated case to ensure a static reference for the velocity fields, and 1 wt. % solutions of PEO was introduced at the same driving pressures ($\text{Re} \approx 10^{-5}$, 10^{-4} and $\text{Wi} = 1.2, 7$). The flow of PEO over PDMS coated bottom surface did not exhibit similar slip as in the case of glass, indicating the chemical nature of the fluidic slip based on surface properties [Fig. 8(c)]. Thus, our experiments and analysis indicate the presence of a finite slip at small shear rates in the case of highly viscoelastic 1 wt. % PEO solution flowing over a glass bottom surface. We also tested PEO solutions of 0.25 and 0.5 wt. % in PDMS/glass devices and did not observe sliplike behavior indicating that this phenomenon is more apparent in semidilute polymer solutions.

Currently, there is lack of consensus on the extent of viscoelastic slip in narrow channels as it may depend on polymer

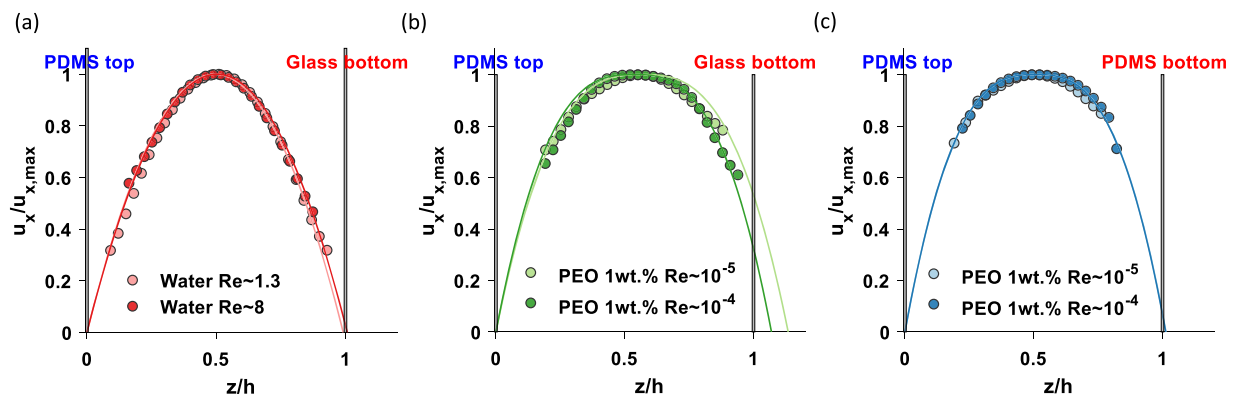


FIG. 8. Characterization of wall slip in microfluidic flows. Normalized depthwise velocity profiles at the midplane for (a) water in a PDMS channel bonded to glass slide, (b) PEO in a PDMS channel bonded to glass slide, and (c) PEO in a PDMS channel bonded to PDMS coated glass slide. The lines are the fits to Eq. (5).

properties, shear rate, and dynamic/static surface inhomogeneities. Experimentally, for flow of water in hydrophobic microchannels, the slip length was reported to be about $1\ \mu\text{m}$ using microPIV.⁷¹ The total internal reflection fluorescence (TIRF)-based techniques show a slip length of $\sim 0.1\ \mu\text{m}$ for Newtonian and viscoelastic fluids⁷² in the range of $200\text{--}800\ \text{s}^{-1}$. In our study, the shear rates are much lower ($\approx 1\ \text{s}^{-1}$), and also the radius of gyration of polymer used is different making it difficult to compare. Molecular dynamics simulations of polymeric shear flows also indicate the presence of slip that is shear-rate dependent,⁷³ but coordinated efforts to compare simulation data to experiments do not exist. The only independent study supporting our slip measurements is that by Degre *et al.*,²⁹ who also observed slip lengths in the micrometer-range with PEO solutions using microPIV. Overall, even though the HSR technique is insensitive to the presence of the wall-slip, these results indicate that slip may occur in microscale viscoelastic flows, and DHM-PTV is a useful means to observe this phenomenon.

2. Particle migration in Newtonian and viscoelastic microslit flows

The acquisition of flow kinematics and subsequent rheometry using DHM PTV requires a nonsparse particle field to permeate the flow volume of interest. It is essential, therefore, to recognize any stratification that may occur due to the effects of particle size, flow rate, particle-particle interactions, confinement, slip, and rheology of the suspending fluid.⁵⁹ As mentioned briefly before, we have observed particle stratification in our experiments, which impacted

our velocity profile characterization. We discuss these experiments and results below.

Particle migration can occur due to solely inertia⁷⁴ as well as due to purely normal stress differences in viscoelastic fluids.⁵⁵ In addition, entry junctions promote focusing in Newtonian flows.^{50,51} We investigated whether particle migration can occur under conditions of our rheology studies where both inertial and viscoelastic effects are present. The particle field was analyzed in the thin-slit geometry by counting the number of particles N_z in horizontal planes (width $\sim 50\ \mu\text{m}$) and normalizing the counts by the total number of particles N_T . Holographic imaging was performed at $\approx 115D_h$ from the entrance, which is enough for flow stabilization but significantly lower than the typical length scales ($>1000D_h$) employed for equilibrium particle focusing.^{59,75–77} As a result, the data shown here do not pertain to equilibrium focusing dynamics of particles.

The particle distribution in the vertical midplane from the centerline to the top wall for water is shown in Fig. 9(a). At low Re (≈ 1), we observe a nearly homogeneous particle distribution along the vertical midplane, whereas at higher Re values (~ 32), the particles are depleted from the core and wall regions and a rise in concentration between the channel center and the walls is detected at approximately $\approx 0.25h$ to $0.3h$ away from the center. The particle distribution for water at low Re is consistent with a reversible Stokesian flow that does not allow migration, whereas the stratification at higher Re originates from inertial nonlinearities.⁷⁴

Next, we consider pressure driven flows of 0.025 wt. % PEO for the viscoelastic case with weak shear thinning as shown in Fig. 9(b).

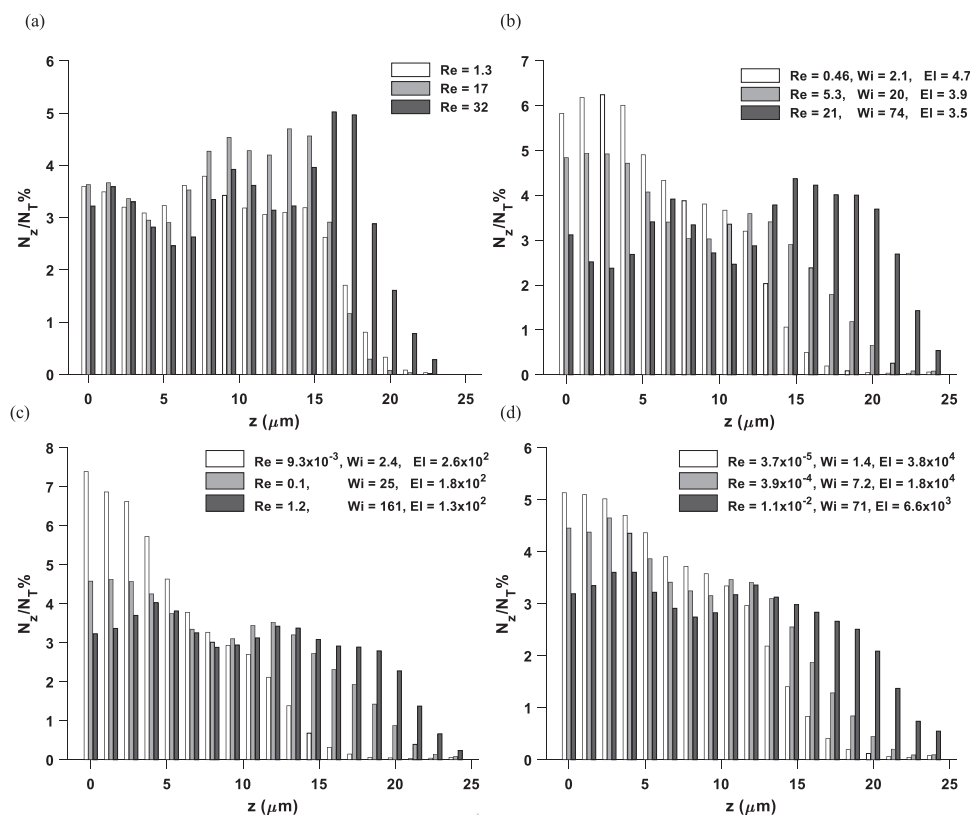


FIG. 9. Particle distributions are shown in the vertical plane from centerline to top-wall for a thin-slit microchannel. Each fluid is tested at three different pressure-driven flow conditions. (a) Water, (b) 0.025 wt. % PEO, (c) 0.25 wt. % PEO, and (d) 1 wt. % PEO.

In the viscoelasticity dominant regime ($Re = 0.46$, $Wi = 2.1$, and $El = 4.7$), the particle distribution is pronounced at the center, indicating a migration induced by the normal-stress difference. In flow with nonnegligible inertia and elasticity ($Re = 5.3$, $Wi = 20$, and $El = 3.9$), the peak in the particle distribution at the center is slightly diminished, whereas a secondary maximum appears at $\sim 0.25h$ to $0.3h$, indicating the competition between viscoelastic and inertial effects in localized reordering of the particle field. Finally, when $Re = 21$ and $Wi = 71$ ($El = 3.5$), particle depletion occurs at the center with a distinct rise between the center and the wall indicating a more prominent role of inertial effects. We also measured particle distributions in 0.25 wt. % and 1 wt. % PEO solutions, which are more viscoelastic and show stronger shear thinning than 0.025 wt. % PEO solution [Figs. 9(c) and 9(d)]. However, the trends in particle distribution are very similar to that of 0.025 wt. % PEO solution.

In viscoelastic weakly shear thinning flows [0.025 wt. % PEO, Fig. 9(b)] at low Re , the observed migration toward regions of the lowest (absolute) shear is similar to a second order fluid.^{55,57} In strongly shear thinning viscoelastic flows [0.25 wt. % and 1 wt. % PEO, Figs. 9(c) and 9(d)], the stratification is again similar to a second order fluid at low Re ; however, at higher Re , the strong shear thinning appears to drive a second maximum between the wall and the center alongside a diminished central peak and redispersion in the distribution profile.

Overall, we find that in holography shear rheology of viscoelastic fluids, particle distribution can be nonuniform, which precludes the sparse velocity vector field, especially close to the walls. Nevertheless, as we have shown HSR is capable of characterizing the shear rheology of viscoelastic fluids.

V. CONCLUSIONS

In summary, we have developed a new tool by adapting an existing DHM-PTV to a viscoelastic experimental system, which we refer to as holographic shear rheology (HSR). We demonstrate a novel implementation of DHM-PTV for simultaneous acquisition of 3D velocity fields, shear rheology, particle distribution, and slip length in viscoelastic flows from 3D imaging of particle-imbued flow volume. The slip behavior is observed in highly viscoelastic PEO solutions at low shear rates with slip lengths in the order of 3–5 μm . We have shown that this HSR approach can characterize shear rheology of viscoelastic fluids across a wide range of shear rates. From a rheometry perspective, HSR obviates the need to have external sensors to measure shear rheology and is not limited by the presence of the wall-slip. The holography system presented here can be further miniaturized^{78,79} with the current microfluidic assembly, potentially leading to compact and portable rheometers. Finally, there is a need to extend the DHM-PTV approach to other complex fluids and geometries. Compared to other velocimetry techniques, the holographic approach does not require mechanical scanning and, therefore, has significant potential to characterize time-resolved 3D velocity fields, opening up new opportunities in viscoelastic fluid mechanics.

ACKNOWLEDGMENTS

The authors would like to thank Dr. Dhananjay Singh and Dr. Naureen Suteria for help with digital reconstruction and DOS

experiments, respectively. We are grateful to Dr. Paul Salipante for the useful discussions regarding particle tracking. Finally, we would like to acknowledge Professor Vinothan Manoharan and his lab for helpful discussions regarding DHM.

REFERENCES

- C. J. Pipe and G. H. McKinley, "Microfluidic rheometry," *Mech. Res. Commun.* **36**(1), 110–120 (2009).
- S. Gupta, W. S. Wang, and S. A. Vanapalli, "Microfluidic viscometers for shear rheology of complex fluids and biofluids," *Biomed. Microfluid.* **10**(4), 043402 (2016).
- F. J. Galindo-Rosales, M. Alves, and M. S. Oliveira, "Microdevices for extensional rheometry of low viscosity elastic liquids: A review," *Microfluid. Nanofluid.* **14**(1–2), 1–19 (2013).
- D. E. Solomon and S. A. Vanapalli, "Multiplexed microfluidic viscometer for high-throughput complex fluid rheology," *Microfluid. Nanofluid.* **16**(4), 677–690 (2014).
- N. Srivastava and M. A. Burns, "Analysis of non-Newtonian liquids using a microfluidic capillary viscometer," *Anal. Chem.* **78**(5), 1690–1696 (2006).
- C. J. Pipe, T. S. Majumdar, and G. H. McKinley, "High shear rate viscometry," *Rheol. Acta* **47**(5–6), 621–642 (2008).
- S. J. Haward *et al.*, "Optimized cross-slot flow geometry for microfluidic extensional rheometry," *Phys. Rev. Lett.* **109**(12), 128301 (2012).
- T. J. Ober *et al.*, "Microfluidic extensional rheometry using a hyperbolic contraction geometry," *Rheol. Acta* **52**(6), 529–546 (2013).
- S. Haward, "Microfluidic extensional rheometry using stagnation point flow," *Biomed. Microfluid.* **10**(4), 043401 (2016).
- D. E. Solomon, A. Abdel-Razik, and S. A. Vanapalli, "A stress-controlled microfluidic shear viscometer based on smartphone imaging," *Rheol. Acta* **55**(9), 727–738 (2016).
- S. D. Hudson *et al.*, "A microliter capillary rheometer for characterization of protein solutions," *J. Pharm. Sci.* **104**(2), 678–685 (2015).
- P. F. Salipante, C. A. Little, and S. D. Hudson, "Jetting of a shear banding fluid in rectangular ducts," *Phys. Rev. Fluids* **2**(3), 033302 (2017).
- P. Arosio *et al.*, "Microfluidic diffusion viscometer for rapid analysis of complex solutions," *Anal. Chem.* **88**(7), 3488–3493 (2016).
- G. Degré *et al.*, "Complex fluids rheology in microchannels using a micro-PIV technique," in 9th International Conference On Miniaturized Systems for Chemistry and Life Sciences, 2005.
- J. Katz and J. Sheng, "Applications of holography in fluid mechanics and particle dynamics," *Annu. Rev. Fluid Mech.* **42**, 531–555 (2010).
- J. Garcia-Sucerquia *et al.*, "Digital in-line holographic microscopy," *Appl. Opt.* **45**(5), 836–850 (2006).
- T. Ooms, R. Lindken, and J. Westerweel, "Digital holographic microscopy applied to measurement of a flow in a T-shaped micromixer," *Exp. Fluids* **47**(6), 941 (2009).
- S. Kim and S. J. Lee, "Measurement of Dean flow in a curved micro-tube using micro digital holographic particle tracking velocimetry," *Exp. Fluids* **46**(2), 255 (2009).
- H. B. Evans *et al.*, "Holographic microscopy and microfluidics platform for measuring wall stress and 3D flow over surfaces textured by micro-pillars," *Sci. Rep.* **6**, 28753 (2016).
- J. Fung *et al.*, "Measuring translational, rotational, and vibrational dynamics in colloids with digital holographic microscopy," *Opt. Express* **19**(9), 8051–8065 (2011).
- J. Fung and V. N. Manoharan, "Holographic measurements of anisotropic three-dimensional diffusion of colloidal clusters," *Phys. Rev. E* **88**(2), 020302 (2013).
- S.-i. Satake *et al.*, "Measurements of 3D flow in a micro-pipe via micro digital holographic particle tracking velocimetry," *Meas. Sci. Technol.* **17**(7), 1647 (2006).
- S.-i. Satake *et al.*, "Three-dimensional flow tracking in a micro channel with high time resolution using micro digital-holographic particle-tracking velocimetry," *Opt. Rev.* **12**(6), 442–444 (2005).

- ²⁴P. Salipante *et al.*, "Microparticle tracking velocimetry as a tool for microfluidic flow measurements," *Exp. Fluids* **58**(7), 85 (2017).
- ²⁵J. Zhang, B. Tao, and J. Katz, "Turbulent flow measurement in a square duct with hybrid holographic PIV," *Exp. Fluids* **23**(5), 373–381 (1997).
- ²⁶J. Sheng, E. Malkiel, and J. Katz, "Using digital holographic microscopy for simultaneous measurements of 3D near wall velocity and wall shear stress in a turbulent boundary layer," *Exp. Fluids* **45**(6), 1023–1035 (2008).
- ²⁷B. Qin *et al.*, "Upstream vortex and elastic wave in the viscoelastic flow around a confined cylinder," *J. Fluid Mech.* **864**, R2 (2019).
- ²⁸N. S. Suteria *et al.*, "eCapillary: a disposable microfluidic extensional viscometer for weakly elastic polymeric fluids," *Rheol. Acta* **58**, 403 (2019).
- ²⁹G. Degré *et al.*, "Rheology of complex fluids by particle image velocimetry in microchannels," *Appl. Phys. Lett.* **89**(2), 024104 (2006).
- ³⁰C. Macosko, *Principles of Rheology: Measurements and Applications* (VCH, New York, 1994).
- ³¹K. Kang, L. J. Lee, and K. W. Koelling, "High shear microfluidics and its application in rheological measurement," *Exp. Fluids* **38**(2), 222–232 (2005).
- ³²M. Ishikawa *et al.*, "A novel algorithm for particle tracking velocimetry using the velocity gradient tensor," *Exp. Fluids* **29**(6), 519–531 (2000).
- ³³J. W. Goodman, *Introduction to Fourier Optics* (Roberts and Company Publishers, 2005).
- ³⁴L. Yu and M. K. Kim, "Wavelength scanning digital interference holography for variable tomographic scanning," *Opt. Express* **13**(15), 5621–5627 (2005).
- ³⁵L. Yu and M. K. Kim, "Wavelength-scanning digital interference holography for tomographic three-dimensional imaging by use of the angular spectrum method," *Opt. Lett.* **30**(16), 2092–2094 (2005).
- ³⁶M. K. Kim, "Principles and techniques of digital holographic microscopy," *SPIE Rev.* **1**(1), 018005 (2010).
- ³⁷T. Kreis, *Handbook of Holographic Interferometry: Optical and Digital Methods* (John Wiley & Sons, 2006).
- ³⁸D. K. Singh and P. Panigrahi, "Three-dimensional investigation of liquid slug Taylor flow inside a micro-capillary using holographic velocimetry," *Exp. Fluids* **56**(1), 6 (2015).
- ³⁹M.-a. Ishikawa, Y. Murai, and F. Yamamoto, "Numerical validation of velocity gradient tensor particle tracking velocimetry for highly deformed flow fields," *Meas. Sci. Technol.* **11**(6), 677 (2000).
- ⁴⁰D. K. Singh *et al.*, "Label-free, high-throughput holographic screening and enumeration of tumor cells in blood," *Lab Chip* **17**(17), 2920–2932 (2017).
- ⁴¹D. K. Singh *et al.*, "Label-free fingerprinting of tumor cells in bulk flow using inline digital holographic microscopy," *Biomed. Opt. Express* **8**(2), 536–554 (2017).
- ⁴²A. M. Shetty and M. J. Solomon, "Aggregation in dilute solutions of high molar mass poly (ethylene) oxide and its effect on polymer turbulent drag reduction," *Polymer* **50**(1), 261–270 (2009).
- ⁴³J. Dinic, L. N. Jimenez, and V. Sharma, "Pinch-off dynamics and dripping-onto-substrate (DoS) rheometry of complex fluids," *Lab Chip* **17**(3), 460–473 (2017).
- ⁴⁴D. C. Duffy *et al.*, "Rapid prototyping of microfluidic systems in poly (dimethylsiloxane)," *Anal. Chem.* **70**(23), 4974–4984 (1998).
- ⁴⁵K. Madlener, B. Frey, and H. Ciezki, "Generalized Reynolds number for non-Newtonian fluids," *Prog. Propul. Phys.* **1**, 237–250 (2009).
- ⁴⁶D. Boger, "Viscoelastic flows through contractions," *Annu. Rev. Fluid Mech.* **19**(1), 157–182 (1987).
- ⁴⁷D. Boger and A. Ramamurthy, "Experimental measurements of loss coefficients in the entrance region of a pipe for viscous power law and viscoelastic fluids," *AIChE J.* **16**(6), 1088–1091 (1970).
- ⁴⁸B. Henrik, *Theoretical Microfluidics* (MIC-Department of micro and Nanotechnology, Technical University of Denmark, 2005), Vol. 2.
- ⁴⁹E. Stoykova, H. Kang, and J. Park, "Twin-image problem in digital holography-a survey," *Chin. Opt. Lett.* **12**(6), 060013 (2014).
- ⁵⁰M. E. Staben, A. Z. Zinchenko, and R. H. Davis, "Motion of a particle between two parallel plane walls in low-Reynolds-number Poiseuille flow," *Phys. Fluids* **15**(6), 1711–1733 (2003).
- ⁵¹M. E. Staben and R. H. Davis, "Particle transport in Poiseuille flow in narrow channels," *Int. J. Multiphase Flow* **31**(5), 529–547 (2005).
- ⁵²G. D'Avino *et al.*, "Single line particle focusing induced by viscoelasticity of the suspending liquid: Theory, experiments and simulations to design a micropipe flow-focuser," *Lab Chip* **12**(9), 1638–1645 (2012).
- ⁵³S. Kim and S. J. Lee, "Effect of particle number density in in-line digital holographic particle velocimetry," *Exp. Fluids* **44**(4), 623–631 (2008).
- ⁵⁴M. Malek *et al.*, "Digital in-line holography: Influence of the shadow density on particle field extraction," *Opt. Express* **12**(10), 2270–2279 (2004).
- ⁵⁵B. Ho and L. Leal, "Migration of rigid spheres in a two-dimensional unidirectional shear flow of a second-order fluid," *J. Fluid Mech.* **76**(4), 783–799 (1976).
- ⁵⁶A. Karnis, H. Goldsmith, and S. Mason, "The flow of suspensions through tubes: V. Inertial effects," *Can. J. Chem. Eng.* **44**(4), 181–193 (1966).
- ⁵⁷A. Karnis and S. Mason, "Particle motions in sheared suspensions. XIX. Viscoelastic media," *Trans. Soc. Rheol.* **10**(2), 571–592 (1966).
- ⁵⁸A. Karnis, H. Goldsmith, and S. Mason, "Axial migration of particles in Poiseuille flow," *Nature* **200**(4902), 159 (1963).
- ⁵⁹G. D'Avino, F. Greco, and P. L. Maffettone, "Particle migration due to viscoelasticity of the suspending liquid and its relevance in microfluidic devices," *Annu. Rev. Fluid Mech.* **49**, 341–360 (2017).
- ⁶⁰F. Del Giudice *et al.*, "Is microrheometry affected by channel deformation?," *Biomicrofluidics* **10**(4), 043501 (2016).
- ⁶¹T. Gervais *et al.*, "Flow-induced deformation of shallow microfluidic channels," *Lab Chip* **6**(4), 500–507 (2006).
- ⁶²R. G. Larson, *The Structure and Rheology of Complex Fluids* (Topics in Chemical Engineering) (Oxford University Press, New York, Oxford, 1999), Vol. 86, p. 108.
- ⁶³T. T. Dao and L. A. Archer, "Stick-slip dynamics of entangled polymer liquids," *Langmuir* **18**(7), 2616–2624 (2002).
- ⁶⁴V. Mhetar and L. Archer, "Slip in entangled polymer melts. 2. Effect of surface treatment," *Macromolecules* **31**(24), 8617–8622 (1998).
- ⁶⁵P. E. Boukany, Y. T. Hu, and S.-Q. Wang, "Observations of wall slip and shear banding in an entangled DNA solution," *Macromolecules* **41**(7), 2644–2650 (2008).
- ⁶⁶K. Migler, H. Hervet, and L. Leger, "Slip transition of a polymer melt under shear stress," *Phys. Rev. Lett.* **70**(3), 287 (1993).
- ⁶⁷P. T. Callaghan, "Rheo-NMR: Nuclear magnetic resonance and the rheology of complex fluids," *Rep. Prog. Phys.* **62**(4), 599 (1999).
- ⁶⁸F. Brochard and P. De Gennes, "Shear-dependent slippage at a polymer/solid interface," *Langmuir* **8**(12), 3033–3037 (1992).
- ⁶⁹J. P. Rothstein, "Slip on superhydrophobic surfaces," *Annu. Rev. Fluid Mech.* **42**, 89–109 (2010).
- ⁷⁰V. Mhetar and L. Archer, "Slip in entangled polymer melts. 1. General features," *Macromolecules* **31**(24), 8607–8616 (1998).
- ⁷¹D. C. Tretheway and C. D. Meinhardt, "Apparent fluid slip at hydrophobic microchannel walls," *Phys. Fluids* **14**(3), L9–L12 (2002).
- ⁷²Z. Li *et al.*, "Slip length measurements using μ PIV and TIRF-based velocimetry," *Isr. J. Chem.* **54**(11–12), 1589–1601 (2014).
- ⁷³N. V. Priezjev, "Shear rate threshold for the boundary slip in dense polymer films," *Phys. Rev. E* **80**(3), 031608 (2009).
- ⁷⁴B. Ho and L. Leal, "Inertial migration of rigid spheres in two-dimensional unidirectional flows," *J. Fluid Mech.* **65**(2), 365–400 (1974).
- ⁷⁵A. M. Leshansky *et al.*, "Tunable nonlinear viscoelastic 'focusing' in a microfluidic device," *Phys. Rev. Lett.* **98**(23), 234501 (2007).
- ⁷⁶K. W. Seo *et al.*, "Particle migration and single-line particle focusing in microscale pipe flow of viscoelastic fluids," *RSC Adv.* **4**(7), 3512–3520 (2014).
- ⁷⁷H. Amini, W. Lee, and D. Di Carlo, "Inertial microfluidic physics," *Lab Chip* **14**(15), 2739–2761 (2014).
- ⁷⁸T. G. Dimiduk, *Holographic Microscopy for Soft Matter and Biophysics* (Harvard University, Graduate School of Arts & Sciences, 2016).
- ⁷⁹T. Shimobaba *et al.*, "Portable and low-cost digital holographic microscopy using web camera, point light source LED and open-source libraries," in *Digital Holography and Three-Dimensional Imaging* (Optical Society of America, 2012).